Multiple k-Point Nonadiabatic Molecular Dynamics for Ultrafast Excitations in Periodic Systems: The Example of Photoexcited Silicon

Fan Zheng[1,*] and Lin-wang Wang[2,†]

[1]School of Physical Science and Technology, ShanghaiTech University, Shanghai 201210, China
[2]State Key Laboratory of Superlattices and Microstructures, Institute of Semiconductors, Chinese Academy of Science, Beijing 100083, China

(Received 21 September 2022; revised 22 March 2023; accepted 18 August 2023; published 10 October 2023)

With the rapid development of ultrafast experimental techniques for the research of carrier dynamics in solid-state systems, a microscopic understanding of the related phenomena, particularly a first-principle calculation, is highly desirable. Nonadiabatic molecular dynamics (NAMD) offers a real-time direct simulation of the carrier transfer or carrier thermalization. However, when applied to a periodic supercell, there is no cross-k-point transitions during the NAMD simulation. This often leads to a significant underestimation of the transition rate with the single-k-point band structure in a supercell. In this work, based on the surface hopping scheme used for NAMD, we propose a practical method to enable the cross-k transitions for a periodic system. We demonstrate our formalism by showing that the hot electron thermalization process by the multi-k-point NAMD in a small silicon supercell is equivalent to such simulation in a large supercell with a single Γ point. The simulated hot carrier thermalization process of the bulk silicon is compared with the recent ultrafast experiments, which shows excellent agreements. We have also demonstrated our method for the hot carrier coolings in the amorphous silicons and the $GaAlAs_2$ solid solutions with the various cation distributions.

DOI: 10.1103/PhysRevLett.131.156302

The ultrafast carrier dynamics in solid states plays a critical role in various areas, such as energy materials [1,2], optoelectronics [3–5], sensors [6], and quantum materials [7]. Benefiting from the rapid developments of spatial and temporal resolutions of the ultrafast experimental techniques, we are now able to trace the very detailed and fundamental dynamical movements of electrons, holes, and ions [8]. However, the development of theoretical tools, in particular first-principle methods, to study the ultrafast carrier transport is lagging behind. The large size of the systems we are interested brings tremendous challenges to the *ab initio* simulations of carrier dynamics. Meanwhile, the complex nature of the physical processes associated with different scattering mechanisms, including the electron-electron, electron-phonon, electron-hole, and carrier-defect scatterings goes beyond the equilibrium condition at which most first-principle calculations are formulated [8]. One solution is to compute the various scatterings explicitly with the first-principle perturbation methods [9,10]. This type of method provides an intuitive and systematic understanding of various couplings in the carrier transport. However, for a complex system with thousands of energy bands and phonon modes such as surfaces, interfaces, or nanomaterials, the perturbation calculation becomes cumbersome and difficult.

Nonadiabatic molecular dynamics (NAMD), originally developed in quantum chemistry field, has become an emerging way to study the ultrafast carrier dynamics in periodic solid states [11–16]. NAMD, such as surface hopping, is carried out by directly evolving the wave functions of excited carriers following the time-dependent Schrödinger's equation [17,18]. Particularly, in solid states, by implementing the classical path approximation (CPA) [19], the surface hopping NAMD becomes a postprocessing of the ground-state *ab initio* molecular dynamics (MD), which simplifies the implementations and reduces the computational cost greatly. Such approximation works well, particularly in solid-state materials, when the carrier excitation is not strong and the wave functions are extended. Based on the CPA, the NAMD simulations become possible in various solid-state dynamical processes, such as charge thermalization [14,20], interfacial carrier transfer [21–25], exciton transfer [26], surface chemical reactions [27,28], and defect trapping [29,30]. However, most NAMD simulations in solid states only allow a supercell with a single Γ-point wave vector. While this setup is generally fine for small nanomaterials, for a periodic bulk MD simulation, the multi-k-point sampling and the electron transfer across the different k points becomes essential. More importantly, in many cases, the single-k-point electronic eigen energies of an affordable supercell has large unphysical "energy gaps," which causes the artificial "phonon bottleneck" and significantly hinders the thermalization process.

In this Letter, we propose a multi-k-point first-principle NAMD approach based on the decoherence induced

 © 2023 American Physical Society

surface hopping (DISH) scheme to capture the electronic transitions between the eigen states across different k points. By using the bulk silicon as an example, we demonstrate that the hot electron thermalization in a small supercell with a multi-k-point sampling is consistent to its equivalent large supercell with a single Γ-point simulation. This approach is further optimized to include the acoustic phonon modes induced by the deformation potential to assist the intraband carrier transport. We show that this calculation yields an excellent agreement with the experiment of the hot carrier cooling in the bulk silicon. Furthermore, with this method, we have compared the carrier cooling processes in the crystalline and amorphous silicons, and investigated the effects of cation distributions to the hot carrier cooling in the solid-solution materials. These systems are usually difficult to simulate with conventional methods.

In a NAMD simulation using a supercell, only zone-center phonon modes are assisting the interstate transitions within one k point. This is realized by computing the nonadiabatic coupling $V_{ij}(t) = \langle \phi_i(t) | [\partial \phi_j(t)/\partial t] \rangle$, where $|\phi_i(t)\rangle$ is the time-dependent adiabatic states (i.e., eigen states of each MD step). First,

$$\begin{aligned} V_{ij}(t) &= \left\langle \phi_i(t) \middle| \frac{\partial \phi_j(t)}{\partial t} \right\rangle \\ &= \sum_{\boldsymbol{R}} \left\langle \phi_i(t) \middle| \frac{\partial \phi_j(t)}{\partial \boldsymbol{R}} \right\rangle \dot{\boldsymbol{R}} \\ &= \sum_{\boldsymbol{R}} \frac{1}{\epsilon_j - \epsilon_i} \left\langle \phi_i(t) \middle| \frac{\partial H}{\partial \boldsymbol{R}} \middle| \phi_j(t) \right\rangle \dot{\boldsymbol{R}}, \end{aligned} \tag{1}$$

where $\boldsymbol{R}(t)$ is the nuclear positions representing the MD trajectory and ϵ_i is the ith eigen energy. In the supercell MD, only the supercell zone-center phonon mode ($U_{\boldsymbol{R}}$ and it is periodic) is available. This expression is also consistent to the explicit electron-phonon coupling matrix element [9]. However, for a multi-k-point scheme, a non-zone-center phonon mode with finite wave vector $\mathbf{q}$ is needed to assist the carrier transition between $\boldsymbol{k}$ and $\boldsymbol{k}'$ (with $\mathbf{q} = \boldsymbol{k} - \boldsymbol{k}'$). Here, we make an approximation of the supercell q-point phonon mode based on the zone-center phonon mode by multiplying a factor of $e^{i\mathbf{q}\cdot\boldsymbol{R}}$ to $U_{\boldsymbol{R}}$. As a result, we have

$$\dot{\boldsymbol{R}} = \frac{1}{\sqrt{N_{\mathbf{q}}}} \sum_{\mathbf{q}} \dot{U}_{\boldsymbol{R}}(t) e^{i\mathbf{q}\cdot\boldsymbol{R}} e^{i\theta_{\mathbf{q}}}, \tag{2}$$

where $\theta_{\mathbf{q}}$ is a random phase, and $N_{\mathbf{q}}$ is the number of $\mathbf{q}$ points. Now, rewrite Eq. (1) by replacing state $|\phi_i\rangle$ to $|\phi_{i\boldsymbol{k}}\rangle$, and plug Eq. (2) into Eq. (1) with $|\phi_{i\boldsymbol{k}}(t)\rangle = 1/\sqrt{N} e^{i\boldsymbol{k}\cdot\boldsymbol{r}} |u_{i\boldsymbol{k}}(t)\rangle$ (N is for proper normalization of $|\phi_{i\boldsymbol{k}}\rangle$), we can derive

$$\begin{aligned} V_{i\boldsymbol{k},j\boldsymbol{k}'}(t) &= \left\langle \phi_{i\boldsymbol{k}}(t) \middle| \frac{\partial \phi_{j\boldsymbol{k}'}(t)}{\partial t} \right\rangle \\ &\approx \frac{1}{\Delta t \sqrt{N_{\mathbf{q}}}} \frac{1}{\epsilon_{j\boldsymbol{k}'}(t+\Delta t) - \epsilon_{i\boldsymbol{k}}(t)} \\ &\quad \times \langle u_{i\boldsymbol{k}}(t) | [H_{\boldsymbol{k}'}(t+\Delta t) - H_{\boldsymbol{k}'}(t)] | u_{j\boldsymbol{k}'}(t+\Delta t) \rangle \\ &\quad \times e^{i\theta_{\boldsymbol{k}'-\boldsymbol{k}}}, \end{aligned} \tag{3}$$

where Δt is the MD time step, $N_{\mathbf{q}}$ equals the number of k points sampled in the supercell's Brillouin zone, and $H_{\boldsymbol{k}'}$ is the Bloch Hamiltonian at $\boldsymbol{k}'$. Note, N has been dropped out since the integration in Eq. (3) is over the supercell. Here, the momentum conservation ($\mathbf{q} = \boldsymbol{k} - \boldsymbol{k}'$) is achieved through Eq. (2). In actual calculations, we find that $\theta_{\boldsymbol{k}'-\boldsymbol{k}}$ does not affect the results significantly; thus it is set to zero. The detailed derivation of Eq. (3) is given in the Supplemental Material (SM) [31–37].

Following the CPA, in practical implementations, an *ab initio* MD simulation of a midsize supercell with a multi-k-point sampling is performed (we want the trajectory to represent enough phonon modes so a small supercell is still used). During each MD step, when two eigen states $|\phi_{i\boldsymbol{k}}(t)\rangle$ and $|\phi_{j\boldsymbol{k}'}(t+\Delta t)\rangle$ have the same k points (i.e., $\boldsymbol{k} = \boldsymbol{k}'$), $V_{ij}(t) = \langle \phi_i(t) | \phi_j(t+\Delta t) \rangle$ is evaluated following the previous approach but subject to a $(1/\sqrt{N_{\mathbf{q}}})$ prefactor [14,21]; when $\boldsymbol{k} \neq \boldsymbol{k}'$, the above Eq. (3) is evaluated. As shown in SM, these couplings are further modified to eliminate the possible spurious numerical large values resulting from an accidental degeneracy between $\epsilon_{i\boldsymbol{k}}$ and $\epsilon_{j\boldsymbol{k}'}$ during the MD (without any empirical parameters). The so-obtained nonadiabatic couplings $V_{i\boldsymbol{k},j\boldsymbol{k}'}$ are then included to the DISH scheme [the equivalent P-matrix method is also performed (SM, Fig. 9)]. By expanding the wave function of the excited carrier on the basis of the adiabatic states from all the k points [$|\psi(t)\rangle = \sum_{i\boldsymbol{k}} c_{i\boldsymbol{k}}(t) |\phi_{i\boldsymbol{k}}(t)\rangle$], such wave function is evolved following the Schrödinger's equation with the time-dependent Hamiltonians built from the nonadiabatic couplings. All we changed here is to provide the cross-k-point couplings $V_{i\boldsymbol{k},j\boldsymbol{k}'}$ without any additional calculation cost.

In order to verify the multi-k-point NAMD scheme, shown in Fig. 1 is a comparison of the NAMD simulated hot electron cooling between a $2 \times 2 \times 2$ silicon cubic supercell (64 atoms) with a $2 \times 2 \times 2$ k-point sampling and a $4 \times 4 \times 4$ cubic supercell (512 atoms) with the single Γ point. We apply the standard DISH (without the cross-k transitions) to the $4 \times 4 \times 4$ supercell and apply the current multi-k scheme to the $2 \times 2 \times 2$ supercell. By setting an excited electron at approximately the same energy for these two systems, NAMD simulations are carried out and the time-dependent energies [$\langle E(t) \rangle = \sum_{i\boldsymbol{k}} |c_{i\boldsymbol{k}}(t)|^2 \epsilon_{i\boldsymbol{k}}(t)$] is monitored. Here, each surface-hopping NAMD trajectory is an independent stochastic simulation and the final mean energy is averaged over all the trajectories [$\bar{E}(t) = 1/N_{\text{traj}} \sum_{i=1}^{N_{\text{traj}}} \langle E_i(t) \rangle$ and

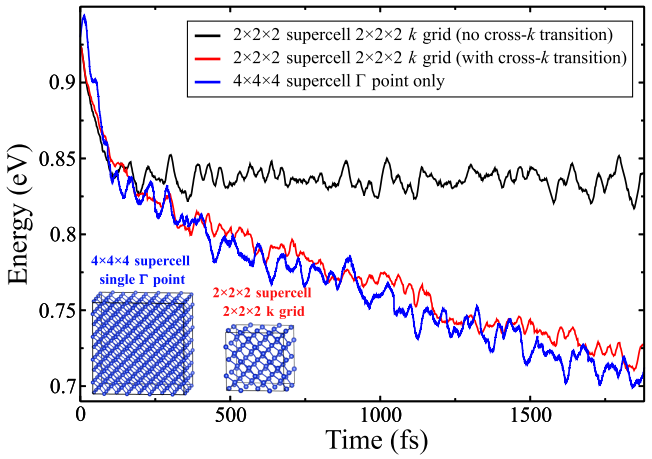

FIG. 1. NAMD simulated mean energies (in terms of CBM) of the electron thermalization processes in the $4 \times 4 \times 4$ Si cubic supercell with a single Γ point and the $2 \times 2 \times 2$ supercell with a $2 \times 2 \times 2$ k-point sampling (without empirical parameters). A simulation for the latter system *without* the cross-k transitions is also shown (black line). To correct the finite-size effect to the eigen-energy fluctuation, the $2 \times 2 \times 2$ supercell MD is carried out at 50 K and the $4 \times 4 \times 4$ supercell case is at 300 K (see SM, Sec. 3). The starting energy for this electron is set around 0.925 eV above CBM.

N_{traj} is the number of trajectories]. By turning on the cross-k transitions in the $2 \times 2 \times 2$ supercell, the simulated hot-carrier energy-cooling profile is almost the same to the $4 \times 4 \times 4$ supercell case throughout the whole thermalization process. This result demonstrates the correctness of our method. In practice, the main computational cost of NAMD with the CPA is the *ab initio* MD part. Compared with the large-supercell single-k-point MD, the small supercell MD with the multiple k points reduces the computational cost significantly due to the DFT-N^3 scaling. Note that based on CPA where the feedback of the excited carrier to the Hamiltonian is ignored, the excitation density will not make a difference for these two systems. Meanwhile, we also test the simulation by turning off the cross-k transitions for the $2 \times 2 \times 2$ supercell with the k-point grid (black line in Fig. 1). The cooling is significantly impeded. In this case, the carrier can only populate the states within this one k point and there are large energy gaps presented in the energy spectrum (see SM, Fig. 5). Other k-point grids are also tested and we find that the $2 \times 2 \times 2$ k grid is already enough to converge the cooling profile (SM, Fig. 12). Here, the finite-size effect on the eigen energy fluctuations during the MD simulation is worth paying attention. Instead of 300 K for the $2 \times 2 \times 2$-supercell MD, we set $T = 50$ K for the NAMD simulation and compensate such different temperature effects to the nonadiabatic couplings. The detailed derivation and determination of the NAMD temperature is discussed in SM, Sec. 3.

So far what is still missing is the role of acoustic phonon modes. Since the finite-box simulation does not contain the $\mathbf{q} = 0$ acoustic modes, these modes are also not considered when multiplying a factor of $e^{i\mathbf{q}\cdot\boldsymbol{R}}$ to the Γ phonon modes to approximate the q-point phonon modes. In Bardeen and Shockley's original paper about the deformation potential [38], the carrier mobility is computed purely based on the acoustic phonon modes induced crystal dilations. Here, on top of the aforementioned formalism, a deformation potential $V^{\text{DP}}_{i\boldsymbol{k},j\boldsymbol{k}'}$ is further added to the nonadiabatic couplings by Eq. (4). Equation (5) is the expression of the coupling strength contributed by the deformation potential [38,39], which is then added to $V_{i\boldsymbol{k},j\boldsymbol{k}'}(t)$ (only when $\boldsymbol{k} \neq \boldsymbol{k}'$) to yield the total couplings $V^{\text{tot}}_{i\boldsymbol{k},j\boldsymbol{k}'}(t)$ used in NAMD:

$$V^{\text{tot}}_{i\boldsymbol{k},j\boldsymbol{k}'}(t) = V_{i\boldsymbol{k},j\boldsymbol{k}'}(t) + V^{\text{DP}}_{i\boldsymbol{k},j\boldsymbol{k}'}(t), \quad \text{when } \boldsymbol{k} \neq \boldsymbol{k}' \tag{4}$$

$$V^{\text{DP}}_{i\boldsymbol{k},j\boldsymbol{k}'}(t) = \frac{1}{\Delta t\sqrt{N_{\mathbf{q}}}} \frac{1}{\epsilon_{j\boldsymbol{k}'}(t+\Delta t) - \epsilon_{i\boldsymbol{k}}(t)} M^{\text{DP}}_{i\boldsymbol{k},j\boldsymbol{k}'} \tag{5}$$

$$M^{\text{DP}}_{i\boldsymbol{k},j\boldsymbol{k}'}(t) = E_1 \sqrt{\frac{k_b T}{2M\omega^2_{\mathbf{q}}}} |\mathbf{q}| \omega_{\mathbf{q}} \Delta t \langle u_{i\boldsymbol{k}}(t) | u_{j\boldsymbol{k}'}(t+\Delta t)\rangle, \tag{6}$$

where E_1 is the deformation potential factor and $\mathbf{q} = \boldsymbol{k} - \boldsymbol{k}'$. M is the mass of silicon atom and $\hbar\omega_{\mathbf{q}}$ is the acoustic phonon mode energy [which is canceled in Eq. (6)]. Here, we assume the acoustic mode is simply $e^{i\mathbf{q}\cdot\boldsymbol{R}}$. We have followed Bardeen's original derivation to arrive in the matrix element in Eq. 6, and in SM Sec. 11 we describe how E_1 is determined. $\langle u_{i\boldsymbol{k}}(t) | u_{j\boldsymbol{k}'}(t+\Delta t)\rangle$ is computed to identify which $j\boldsymbol{k}'$ state belongs to the same band of $i\boldsymbol{k}$ state, hence contributes to the intraband transitions. This term can be calculated on the fly during an MD simulation.

In our actual NAMD simulations, the DISH algorithm implementation is based on the overlap matrix element $S_{i\boldsymbol{k},j\boldsymbol{k}'} = \langle u_{i\boldsymbol{k}}(t) | u_{j\boldsymbol{k}'}(t+\Delta t)\rangle$ (here, $\boldsymbol{k}$ is considered as a state index). Such overlap matrix $S_{i\boldsymbol{k},j\boldsymbol{k}'}$ should satisfy the normalization rule that might be missing due to the approximation. We have applied an orthonormalization procedure as described in SM Sec. 8 before using it in DISH algorithm. Shown in Fig. 2 is the comparison of electron thermalization with and without the deformation potential. By adding the deformation potential, the electron cooling rate is accelerated significantly. Along the whole thermalization process, the energy relaxation rate is not constant, and the cooling rate is around 2 eV/ps for initial 200 fs but reduces to 0.5 eV/ps for the last 400 fs. The relative change of cooling rate is directly related to the density of states (SM, Fig. 5). By adding the deformation potential, it assists the excited carrier wave functions to spread to more states belonging to different k points. Thus, while the optical phonon modes might thermalize the electron by reducing its mean energy, the supercell acoustic phonon modes also prompt the distribution of the carriers among states with similar energies. The hot electron is also

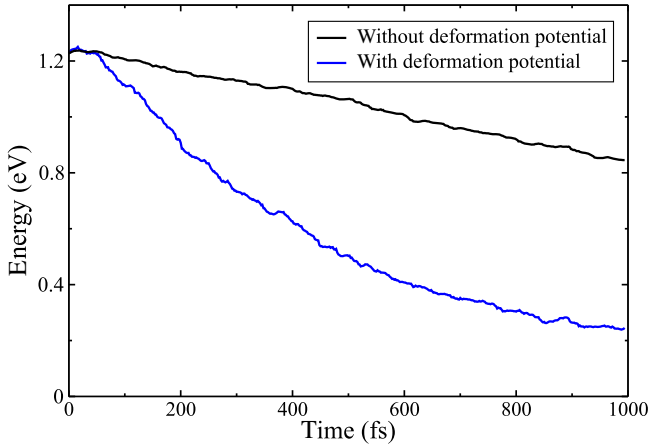

FIG. 2. NAMD simulation of electron thermalizations with the deformation potential. This calculation is performed on a $2 \times 2 \times 2$ silicon supercell with a $2 \times 2 \times 2$ k-point grid.

starting from a different state (of different k points) with a similar energy, but they show unchanged nature of the cooling (SM, Fig. 15).

Application 1: Compare with the experiments.—A well-calibrated carrier relaxation experiment is very challenging. Only recently such experiments become available. Tanimura *et al.* have carried out an experiment for the hot carrier thermalizations in the bulk silicon [40]. In our calculation, we manually populate the states based on the experimentally measured population very shortly after the pump [40]. With this initial population, we perform the NAMD and compare the calculated population change after a finite time with the experimental measurements (the population on state $i\boldsymbol{k}$ is defined as $|c_{i\boldsymbol{k}}(t)|^2$). Shown in Fig. 3 is the time evolution of the state population from time $t = 0$ fs to $t = 600$ fs. At $t = 440$ fs when the

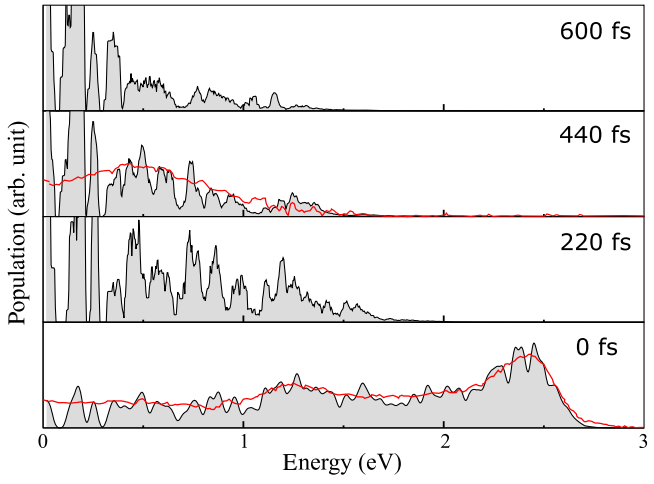

FIG. 3. A NAMD simulated populations of hot electrons in bulk silicon. Time $t = 0$ fs is set manually to be consistent to the measured electron population from the experiment [40]. The red lines are reproduced from Ref. [40]. Energy 0 is the CBM.

experimental result is available, the agreement is very good [40]. We do note that near the conduction band minimum (CBM) (within 0.2 eV), we have a slightly larger population. This is because experimentally below the CBM there are defect and surface states that attract the electron occupations [40].

Application 2: Hot carrier cooling in amorphous silicon.—Given the difficulties of measuring the hot carrier cooling profile in bulk materials, various experimental techniques yield quite different results for the amorphous silicon. References [41,42] present an approximate 2 eV/ps cooling for the amorphous silicon, which are slightly slower compared to the crystalline silicon. But other measurements show that the cooling rate in the amorphous silicon is more rapid than that in the crystalline case [43]. Here, by using the bond-switching method [44], we have built the amorphous silicon supercell (64 atoms supercell), and compare the hot carrier cooling in the amorphous crystal with the aforementioned crystalline results (both are simulated with the same procedure without any empirical parameter). For a defective, amorphous, or disordered system, if the wave function can not be localized within such supercell, a multi k-point setup is still required. Figure 4(a) shows that for both calculations with or without the deformation potential, the amorphous case shows a faster cooling rate than the crystalline one. In addition to the overall thermalization process, the availability of the real-time electron and hole's wave functions allows for a direct investigation of the ultrafast process. We find that the amorphous silicon shows a much stronger real-time oscillator strength than the crystalline one (detailed mechanism in SM, Sec. 16).

Application 3: Vegard's law for hot carrier cooling.—Vegard's law [45] has been used extensively to predict the properties of solid solutions based on the composition ratio [46,47]. However, the applicability of Vegard's law to the hot carrier cooling in solid solutions is never explored. Here, we investigate the carrier cooling of the bulk GaAs and AlAs, and their solid-solution $GaAlAs_2$. Based on the $2 \times 2 \times 2$ cubic GaAs supercell, four different cation arrangements with 50% Ga and 50% Al [Fig. 4(b)] are explored. Figures 4(c) and (d) illustrate the time-dependent mean energies of the hot electron and hole for these four structures and the bulk GaAs and AlAs. Various experiments have shown the hot electron in GaAs thermalizes to the band edge within several picoseconds, and the hole usually presents a faster thermalization rate [48–51], which are both consistent to what we have obtained for GaAs. The cooling profiles of the solid-solution systems show a sensitive dependence on the exact alloy configuration. Although GaAs and AlAs are 50% mixed, the electrons and holes do not show a trend along the median values between those of GaAs and AlAs, as stated by the generalized Vegard's law. Therefore, the Vegard's law

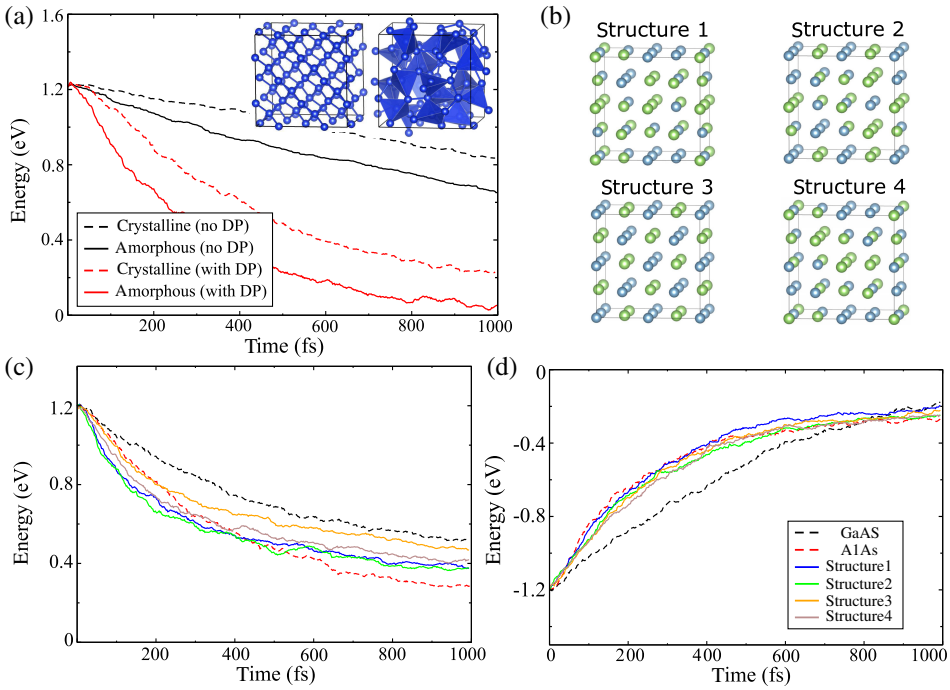

FIG. 4. (a) A comparison of the hot electron coolings in the crystalline and amorphous silicons. The inset figure shows the atomic structures of these two systems. (b) Four structures of solid-solution $GaAlAs_2$ with random arrangements of Ga (green) and Al (light blue) (As atoms are not shown). The mean energies (in terms of CBM for electron or VBM for hole) of the electron (c) and hole (d) cooling as a function of time. All the starting energies are around 1.2 eV above (below) CBM (VBM) for each material.

may not be applied to the hot carrier cooling situations. Here, we want to comment that it will be very challenging to compute the electron-phonon couplings and estimate the carrier cooling rate for the complex systems (e.g., amorphous, defects, alloys, surfaces, and interfaces). Our method presents an advantage to simulate the ultrafast carrier dynamics in these systems.

In summary, we propose a first-principle method to directly simulate the hot carrier thermalization process in periodic bulk systems. An approximated cross-k coupling term is introduced without additional costs. Using the bulk silicon as an example, by enabling the cross-k nonadiabatic couplings, a NAMD simulation performed on a small supercell sampled with multiple k points agrees well with the regular NAMD performed on a large supercell with a single Γ point. By adding the deformation potential, our simulated bulk silicon hot electron thermalization agrees excellently with the most recent experiments. For other systems, without any fitting parameters, this method is also applied to the amorphous silicon and solid solutions of $GaAlAs_2$. Both are difficult to study using the conventional methods. In addition to the hot carrier cooling, this method is applicable to various carrier transfer phenomena in solid states, which provides an efficient tool to investigate the ultrafast dynamic processes.

F. Z. acknowledges the support from the start-up package from ShanghaiTech University. L. W. W. was supported by the National Natural Science Foundation of China, Grant No. T2293700, No. T2293702. The computational support was provided by the HPC Platform of ShanghaiTech University.

*zhengfan@shanghaitech.edu.cn
†lwwang@semi.ac.cn

[1] A. J. Heeger, Adv. Mater. **26**, 10 (2014).
[2] J. Shi, Y. Li, Y. Li, D. Li, Y. Luo, H. Wu, and Q. Meng, Joule **2**, 879 (2018).
[3] V. A. Jhalani, J.-J. Zhou, and M. Bernardi, Nano Lett. **17**, 5012 (2017).
[4] S. Gupta, J. Whitaker, and G. Mourou, IEEE J. Quantum Electron. **28**, 2464 (1992).
[5] M. J. Bowers II, J. R. McBride, M. D. Garrett, J. A. Sammons, A. D. Dukes III, M. A. Schreuder, T. L. Watt, A. R. Lupini, S. J. Pennycook, and S. J. Rosenthal, J. Am. Chem. Soc. **131**, 5730 (2009).
[6] B. Born, J. D. A. Krupa, S. Geoffroy-Gagnon, I. R. Hristovski, C. M. Collier, and J. F. Holzman, ACS Photonics **3**, 2475 (2016).
[7] J. M. Dawlaty, S. Shivaraman, M. Chandrashekhar, F. Rana, and M. G. Spencer, Appl. Phys. Lett. **92**, 042116 (2008).
[8] F. Rossi and T. Kuhn, Rev. Mod. Phys. **74**, 895 (2002).
[9] F. Giustino, Rev. Mod. Phys. **89**, 015003 (2017).
[10] M. Bernardi, D. Vigil-Fowler, J. Lischner, J. B. Neaton, and S. G. Louie, Phys. Rev. Lett. **112**, 257402 (2014).
[11] C. F. Craig, W. R. Duncan, and O. V. Prezhdo, Phys. Rev. Lett. **95**, 163001 (2005).

[12] R. Long and O. V. Prezhdo, J. Am. Chem. Soc. **133**, 19240 (2011).
[13] R. Long and O. V. Prezhdo, J. Am. Chem. Soc. **136**, 4343 (2014).
[14] J. Kang and L.-W. Wang, Phys. Rev. B **99**, 224303 (2019).
[15] Q. Zheng, W. Chu, C. Zhao, L. Zhang, H. Guo, Y. Wang, X. Jiang, and J. Zhao, WIREs Comput. Mol. Sci. **9**, e1411 (2019).
[16] S. Banerjee, J. Kang, X. Zhang, and L.-W. Wang, J. Chem. Phys. **152**, 091102 (2020).
[17] R. Crespo-Otero and M. Barbatti, Chem. Rev. **118**, 7026 (2018).
[18] B. F. E. Curchod and T. J. Martínez, Chem. Rev. **118**, 3305 (2018).
[19] A. V. Akimov and O. V. Prezhdo, J. Chem. Theory Comput. **10**, 789 (2014).
[20] X. Zhou, M. V. Tokina, J. A. Tomko, J. L. Braun, P. E. Hopkins, and O. V. Prezhdo, J. Chem. Phys. **150**, 184701 (2019).
[21] F. Zheng and L.-W. Wang, J. Phys. Chem. Lett. **10**, 6174 (2019).
[22] Z. Wang, P. Altmann, C. Gadermaier, Y. Yang, W. Li, L. Ghirardini, C. Trovatello, M. Finazzi, L. Duò, M. Celebrano, R. Long, D. Akinwande, O. V. Prezhdo, G. Cerullo, and S. Dal Conte, Nano Lett. **21**, 2165 (2021).
[23] J. Zhang, M. Guan, J. Lischner, S. Meng, and O. V. Prezhdo, Nano Lett. **19**, 3187 (2019).
[24] Q. Zheng, W. A. Saidi, Y. Xie, Z. Lan, O. V. Prezhdo, H. Petek, and J. Zhao, Nano Lett. **17**, 6435 (2017).
[25] R. Long and O. V. Prezhdo, Nano Lett. **16**, 1996 (2016).
[26] X. Jiang, Q. Zheng, Z. Lan, W. A. Saidi, X. Ren, and J. Zhao, Sci. Adv. **7**, eabf3759 (2021).
[27] F. Zheng and L.-w. Wang, APL Mater. **8**, 041115 (2020).
[28] W. Chu, S. Tan, Q. Zheng, W. Fang, Y. Feng, O. V. Prezhdo, B. Wang, X.-Z. Li, and J. Zhao, Sci. Adv. **8**, eabo2675 (2022).
[29] W. Chu, W. A. Saidi, J. Zhao, and O. V. Prezhdo, Angew. Chem., Int. Ed. **59**, 6435 (2020).
[30] L. Zhang, W. Chu, Q. Zheng, A. V. Benderskii, O. V. Prezhdo, and J. Zhao, J. Phys. Chem. Lett. **10**, 6151 (2019).
[31] See Supplemental Material, which includes Refs. [32–37], at http://link.aps.org/supplemental/10.1103/PhysRevLett.131.156302 for discussions about the detailed derivations, computational details, size effect, detailed implementation of DISH, convergence tests, and application details of the amorphous and solid-solution materials, etc.
[32] W. Jia, Z. Cao, L. Wang, J. Fu, X. Chi, W. Gao, and L.-W. Wang, Comput. Phys. Commun. **184**, 9 (2013).
[33] W. Jia, J. Fu, Z. Cao, L. Wang, X. Chi, W. Gao, and L.-W. Wang, J. Comput. Phys. **251**, 102 (2013).
[34] J. P. Perdew, K. Burke, and M. Ernzerhof, Phys. Rev. Lett. **77**, 3865 (1996).
[35] D. R. Hamann, Phys. Rev. B **88**, 085117 (2013).
[36] H. M. Jaeger, S. Fischer, and O. V. Prezhdo, J. Chem. Phys. **137**, 22A545 (2012).
[37] A. V. Akimov and O. V. Prezhdo, J. Phys. Chem. Lett. **4**, 3857 (2013).
[38] J. Bardeen and W. Shockley, Phys. Rev. **80**, 72 (1950).
[39] F. Murphy-Armando, G. Fagas, and J. C. Greer, Nano Lett. **10**, 869 (2010).
[40] H. Tanimura, J. Kanasaki, K. Tanimura, J. Sjakste, and N. Vast, Phys. Rev. B **100**, 035201 (2019).
[41] M. Wraback and J. Tauc, Phys. Rev. Lett. **69**, 3682 (1992).
[42] J. O. White, S. Cuzeau, D. Hulin, and R. Vanderhaghen, J. Appl. Phys. **84**, 4984 (1998).
[43] D. Hulin, A. Mourchid, P. Fauchet, W. Nighan, and R. Vanderhagen, J. Non-Cryst. Solids **137–138**, 527 (1991).
[44] F. Zheng, H. H. Pham, and L.-W. Wang, Phys. Chem. Chem. Phys. **19**, 32617 (2017).
[45] A. R. Denton and N. W. Ashcroft, Phys. Rev. A **43**, 3161 (1991).
[46] M. Serényi, C. Frigeri, and R. Schiller, J. Alloys Compd. **763**, 471 (2018).
[47] Y.-K. Kuo, B.-T. Liou, S.-H. Yen, and H.-Y. Chu, Opt. Commun. **237**, 363 (2004).
[48] P. Langot, N. Del Fatti, D. Christofilos, R. Tommasi, and F. Vallée, Phys. Rev. B **54**, 14487 (1996).
[49] Y. Zhang, G. Conibeer, S. Liu, J. Zhang, and J.-F. Guillemoles, Prog. Photovoltaics **30**, 581 (2022).
[50] J. Shah, A. Pinczuk, A. C. Gossard, and W. Wiegmann, Phys. Rev. Lett. **54**, 2045 (1985).
[51] R. W. Schoenlein, W. Z. Lin, E. P. Ippen, and J. G. Fujimoto, Appl. Phys. Lett. **51**, 1442 (1987).